Inorganic Chemistry
Article
Cite This: Inorg. Chem. 2018, 57, 9425−9438
pubs.acs.org/IC

Catalytic Nitrene Homocoupling by an Iron(II) Bis(alkoxide) Complex: Bulking Up the Alkoxide Enables a Wider Range of Substrates and Provides Insight into the Reaction Mechanism

Maryam Yousif,[†] Duleeka Wannipurage,[†] Caleb D. Huizenga,[‡] Elizabeth Washnock-Schmid,[‡] Nicholas J. Peraino,[†,⊥] Andrew Ozarowski,[§] Sebastian A. Stoian,[*,∥] Richard L. Lord,[*,‡] and Stanislav Groysman[*,†]

[†]Department of Chemistry, Wayne State University, 5101 Cass Avenue, Detroit, Michigan 48202, United States
[‡]Department of Chemistry, Grand Valley State University, Allendale, Michigan 49401, United States
[§]National High Magnetic Field Laboratory, Florida State University, Tallahassee, Florida 32310, United States
[∥]Department of Chemistry, University of Idaho, Moscow, Idaho 83844, United States

Supporting Information

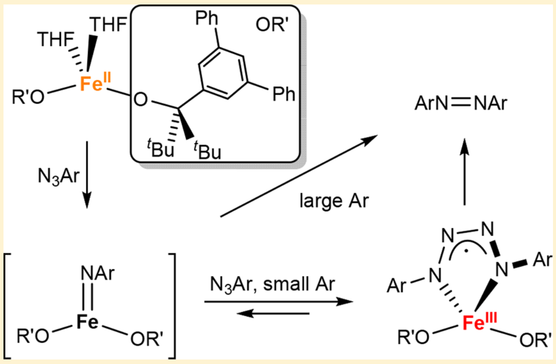

ABSTRACT: The reaction of HOR′ (OR′ = di-t-butyl-(3,5-diphenylphenyl)methoxide) with an iron(II) amide precursor forms the iron(II) bis(alkoxide) complex $Fe(OR')_2(THF)_2$ (**2**). **2** (5−10 mol %) serves as a catalyst for the conversion of aryl azides into the corresponding azoarenes. The highest yields are observed for aryl azides featuring two ortho substituents; other substitution patterns in the aryl azide precursor lead to moderate or low yields. The reaction of **2** with stoichiometric amounts (2 equiv) of the corresponding aryl azide shows the formation of azoarenes as the only organic products for the bulkier aryl azides (Ar = mesityl, 2,6-diethylphenyl). In contrast, formation of tetrazene complexes $Fe(OR')_2(ArNNNNAr)$ (**3**−**6**) is observed for the less bulky aryl azides (Ar = phenyl, 4-methylphenyl, 4-methoxyphenyl, 3,5-dimethylphenyl). The electronic structure of selected tetrazene complexes was probed by spectroscopy (field-dependent ^{57}Fe Mössbauer and high-frequency EPR) and density functional theory calculations. These studies revealed that $Fe(OR')_2(ArNNNNAr)$ complexes contain high-spin ($S = 5/2$) iron(III) centers exchange-coupled to tetrazene radical anions. Tetrazene complexes $Fe(OR')_2(ArNNNNAr)$ produce the corresponding azoarenes (ArNNAr) upon heating. Treatment of a tetrazene complex $Fe(OR')_2(ArNNNNAr)$ with a different azide (N_3Ar') produces all three possible products ArNNAr, ArNNAr′, and Ar′NNAr′. These experiments and quantum mechanics/molecular mechanics calculations exploring the reaction mechanism suggest that the tetrazene functionality serves as a masked form of the reactive iron mono(imido) species.

1. INTRODUCTION

Azoarenes have broad applications in the chemical industry as dyes and pigments; emerging applications include molecular photoswitches, optical storage media, and drug delivery agents.[1−4] Azoarenes are synthesized by a multitude of protocols including azo coupling reactions, condensation of nitroso compounds with anilines, oxidation of anilines using stoichiometric amounts of chemical oxidants, and reductive coupling of nitro compounds.[5] Many of these routes require stoichiometric amounts of chemical oxidants (reductants) and therefore produce significant amounts of waste. Transition-metal mediated catalytic nitrene coupling offers a more general and sustainable route to azoarenes. Transition-metal nitrene chemistry generally originates in organoazides, readily synthesizable and versatile precursors, which undergo two-electron reductive splitting to give a metal-imido functionality and dinitrogen.[6,7] When installed at middle and late transition metals, nitrenes adopt a reactive electrophilic nature, making them capable of coupling with alkenes or isocyanides, or undergoing C−H bond activation to form amines.[8−11] Nitrene homocoupling (dimerization) is a common side reaction in reactive nitrene chemistry.[12] However, metal-imido complexes exhibiting nitrene homocoupling as a primary reaction route are relatively rare, particularly in a catalytic fashion. Hillhouse, Cundari, and co-workers described formation of azomesitylene with a nickel-diphosphine complex, albeit the reaction was not catalytic due to product inhibition.[13] Peters and co-workers have described $[SiP^{iPr}_3]$ iron and ruthenium systems which were catalytically competent to convert several aryl azides ArN_3 (Ar = Ph, 4-MePh, 4-MeOPh, Mes) to azoarenes in moderate yields.[14] Mechanistic investigations led the authors

Received: May 23, 2018
Published: July 17, 2018

DOI: 10.1021/acs.inorgchem.8b01418
Inorg. Chem. 2018, 57, 9425−9438

to conclude that the two systems exhibit different mechanisms: bimolecular metal-nitrene coupling for Fe and "free nitrene" coupling for Ru. Heyduk and co-workers reported catalytic conversion of phenyl azide to azobenzene (10 equiv) using a tantalum catalyst with the redox-active amine bis(phenoxide) ligand.[15] Very recently, Uyeda and co-workers reported a highly efficient dinickel catalyst for the formation of azoarenes.[16] Uyeda's catalyst exhibited broad substrate scope, with the only limitation being bulky groups in the ortho positions (>Mes). The authors showed that this steric inhibition of catalysis results from the inability of bulky aryl nitrenes to react with the second equivalent of a bulky azide. The search for new and efficient catalysts with broad substrate scope is ongoing.

Our group investigates group-transfer reactivity of organoazides and related substrates at transition metal centers in weak-field bis(alkoxide) ligand environments.[17] We have recently demonstrated that an iron bis(alkoxide) complex $Fe(OR)_2(THF)_2$ ($OR = OC^tBu_2Ph$, **1**, Figure 1) catalyzes efficiently the transformation of bulky aryl azides ArN_3 ($Ar = 2,4,6\text{-}Me_3Ph$ or $2,6\text{-}Et_2Ph$) to the corresponding azoarenes.[18] Intriguingly, no azoarene formation was observed for smaller aryl azides (Ar = 2-MePh, 3,5-Me_2Ph, 4-MePh). Instead, formation of bridging imido mono(alkoxide) complexes $Fe_2(\mu_2\text{-}NAr)_2(OR)_2(THF)_2$ was observed, along with tris(alkoxide) byproduct $Fe(OR)_3$. We postulated that alkoxide disproportionation was responsible for the lack of catalysis with smaller aryl azides. To prevent this disproportionation and to shed light into the reaction mechanism, we synthesized the bulkier alkoxide [OR′] ($OR' = OC^tBu_2(3,5\text{-}Ph_2Ph)$) (Figure 2).[19] We anticipated that the larger size of [OR′] would preclude the formation of hypothetical "$Fe(OR')_3$" species, and as a result would prevent alkoxide disproportionation and enable broader catalytic performance with organoazides. Herein we report the synthesis and reactivity of $Fe(OR')_2(THF)_2$ with aryl azides. We specifically show that, due to the lack of alkoxide disproportionation/formation of $Fe(OR')_3$ species, even smaller aryl azides are transformed into azoarenes, albeit less efficiently than bulkier azides (i.e., mesityl). We also demonstrate that the reaction proceeds via the formation of iron-tetrazene intermediates, which were isolated and characterized structurally and spectroscopically.

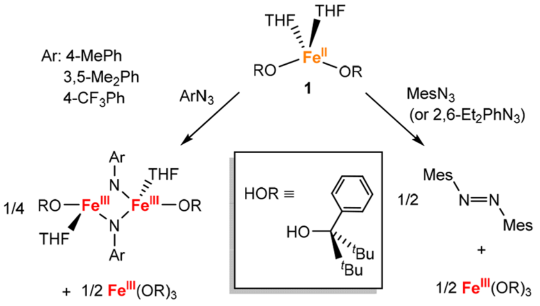

Figure 1. Reactivity of complex **1** with aryl azides as a function of Ar group substituents.

2. METHODS AND MATERIALS

2.1. General Methods and Procedures. All reactions involving air-sensitive materials were executed in a nitrogen-filled glovebox. The synthesis of HOR′ has been previously reported.[19] Mesityl azide, 2-isopropylphenyl azide, 4-isopropylphenyl azide, 2,6-diethylphenyl azide, 3,5-dimethylphenyl azide, 2-phenylphenyl azide, 2-ethylphenyl azide, 2-methoxyphenyl azide, and $Fe[N(SiMe_3)_2]_2(THF)$ were synthesized according to previously reported procedures.[20−23] (Caution: organic azides are potentially shock-sensitive and should be handled with care!) Iron(II) chloride was purchased from Strem. Potassium bis(trimethylsilyl)amide, azidobenzene solution, 4-azidotoluene, 4-(trifluoromethyl)phenyl azide solution, 4-azidoanisole solution, and 2-methylphenyl azide were purchased from Aldrich and used as received. All solvents were purchased from Fisher Scientific and were of HPLC grade. The solvents were purified using an MBraun solvent purification system and stored over 3 Å molecular sieves. Complexes **2**, **4**, and **5** were identified by X-ray crystallography. Compounds **2**−**6** were characterized by IR spectroscopy, solution magnetic susceptibility, and elemental analysis. NMR spectra were recorded at the Lumigen Instrument Center (Wayne State University) on a Varian Mercury 400 MHz NMR spectrometer in C_6D_6 at room temperature. Chemical shifts and coupling constants (*J*) are reported in parts per million (δ) and hertz, respectively. IR spectra of powdered samples were recorded on a Shimadzu IR Affinity-1 Fourier transform (FT-IR) spectrometer outfitted with a MIRacle10 attenuated total reflectance accessory with a monolithic diamond crystal stage and pressure clamp. Magnetic moments were determined using the Evans method.[24] Low resolution mass spectra were obtained at the Lumigen Instrument Center utilizing a Waters Micromass ZQ mass spectrometer (direct injection, with capillary at 3.573 kV and cone voltage of 20.000 V). Only selected peaks in the mass spectra are reported below. Elemental analyses were performed by Midwest Microlab LLC. GCMS was performed at the Lumigen Instrument Center using an Agilent 6890N spectrometer.

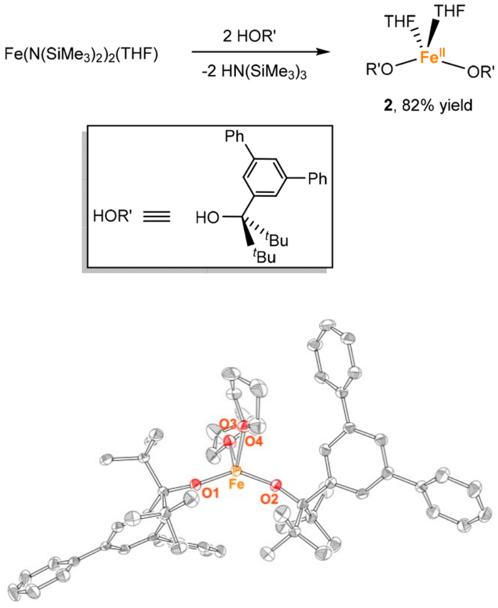

Figure 2. Top: synthesis of $Fe(OR')_2(THF)_2$ (**2**). Bottom: X-ray structure of compound **2**, 50% probability ellipsoids. Selected bond distances (Å) and angles (deg): Fe O1 1.854(2), Fe1 O2 1.828(2), Fe O3 2.177(2), Fe O4 2.179(2), O2 Fe O1 141.5(1), O3 Fe O4 90.2(1).

2.2. Synthesis of Iron Complexes. *2.2.1. $Fe(OR')_2(THF)_2$ (**2**).* To a solution of 5.0 mL of $Fe[N(SiMe)_3]_2(THF)$ (47.8 mg, 0.107 mmol) in THF, HOR′ (69.0 mg, 0.185 mmol) in THF was added slowly. The solution gradually changed color from muddy green to light gold-brown. The reaction was stirred for 2 h, upon which the solvents were removed in vacuo to yield light gold residue. Crystallization from hexanes at −35 °C overnight gave crystals of light gold of **2** (82.3 mg, 82%). IR (cm^{-1}): 2878 (m), 1589 (m), 1416 (m), 1138 (m), 1103 (s), 1018 (s), 979 (s), 872 (m), 760 (d), 694 (s). $\mu_{eff} = 4.7 \pm 0.4\ \mu_B$ Anal. Calcd: C, 79.0; H, 8.3. Found: C, 78.7; H, 8.2.

DOI: 10.1021/acs.inorgchem.8b01418
Inorg. Chem. 2018, 57, 9425−9438

*2.2.2. Fe(OR′)$_2$(PhNNNNPh) (**3**).* To a solution of 3.0 mL of Fe(OR′)$_2$(THF)$_2$ (32.0 mg, 0.0339 mmol) in toluene, azidobenzene (0.14 mL, 0.5 M) in toluene was added slowly. The solution changed color immediately from light gold to deep green-black. The reaction was stirred for 30 min, upon which the solvents were removed in vacuo to yield green-black residue. Crystallization from ether at −35 °C over 2 days gave green-black crystals of **3** (11.5 mg, 34%). IR (cm^{-1}): 2920 (m), 1524 (s), 1489 (s), 1454 (s), 1339 (s), 1123 (m), 1057 (s), 976 (s), 849 (s). $\mu_{\text{eff}} = 4.3 \pm 0.4\ \mu_B$. Anal. Calcd: C, 78.6; H, 7.2; N, 5.6. Found: C, 78.4; H, 7.3; N, 5.5.

*2.2.3. Fe(OR′)$_2$((4-$CH_3C_6H_4$)NNNN(4-$CH_3C_6H_4$)) (**4**).* To a solution of 3.0 mL of Fe(OR′)$_2$(THF)$_2$ (40.9 mg, 0.0434 mmol) in toluene, 4-azidotoluene (0.17 mL, 0.5 M) in toluene was added slowly. The solution changed color immediately from light gold to deep green-black. The reaction was stirred for 30 min, upon which the solvents were removed in vacuo to yield green black residue. Crystallization from ether at −35 °C over 2 days gave dark green crystals of **4** (23.2 mg, 52%). IR (cm^{-1}): 2970 (m), 1593 (s), 1489 (m), 1416 (s), 1389 (s), 1177 (s), 1119 (m), 1045 (s), 1003 (s), 880 (s), 822 (s), 823 (s), 703 (s). $\mu_{\text{eff}} = 4.3 \pm 0.4\ \mu_B$. Calcd: C, 78.7; H, 7.4; N, 5.4. Found: C, 78.4; H, 7.5; N, 5.1.

*2.2.4. Fe(OR′)$_2$((4-$OCH_3C_6H_4$)NNNN(4-$OCH_3C_6H_4$)) (**5**).* To a solution of 3.0 mL of Fe(OR′)$_2$(THF)$_2$ (40.5 mg, 0.0429 mmol) in toluene, 4-azidoanisole (0.20 mL, 0.5M) in toluene was added slowly. The solution changed color immediately from light gold to deep green black. The reaction was stirred for 1 h, upon which the solvents were removed in vacuo to yield green black residue. Crystallization from ether at −35 °C over 2 days gave crystals of dark green crystals of **5** (21.0 mg, 46%). IR (cm^{-1}): 2955 (m), 1497 (m), 1389 (s), 1370 (s), 1246 (m), 1057 (m), 880 (s), 760 (s), 698 (s). $\mu_{\text{eff}} = 4.1 \pm 0.4\ \mu_B$. Anal. Calcd: C, 76.4; H, 7.2; N, 5.2. C, 76.0; H, 7.4; N, 5.2.

*2.2.5. Fe(OR′)$_2$((3,5-$Me_2C_6H_3$)NNNN(3,5-$Me_2C_6H_3$)) (**6**).* To a solution of 3.0 mL of Fe(OR′)$_2$(THF)$_2$ (41.9 mg, 0.044 mmol) in toluene, 3,5-dimethylphenyl azide (1.4 mg, 0.09 mmol) in toluene was added slowly. The solution changed color immediately from light gold to deep green black. The reaction was stirred for 30 min, upon which the solvents were removed in vacuo to yield green-black residue. Crystallization from hexanes at −35 °C over 2 days gave dark green crystals of **6** (31.3 mg, 68%). IR (cm^{-1}): 2970 (m), 1593(s), 1489 (m), 1119 (m), 1045 (s), 999 (s), 880 (s), 822 (s), 768 (s), 702 (s). $\mu_{\text{eff}} = 4.4 \pm 0.4\ \mu_B$. Calcd: C, 78.9; H, 7.6; N, 5.3. Found: C, 79.1; H, 8.0; N, 5.1.

2.3. General Procedure for Catalytic Formation of Azoarenes. All of the reactions were performed by adding 10 or 20 equiv of organic azide and 1,3,5-trimethoxybenzene (TMB) standard solution in C_6D_6 to a solution of complex **2** (approximately 30−35 mg) in C_6D_6 in an N_2-filled glovebox. The reaction mixture was then stirred at the noted temperature for 8 or 24 h. The yields of azoarene products were determined by ^{1}H NMR spectroscopy and GCMS (see Supporting Information).

2.4. Formation of Azoarene from Tetrazene Complex. A solution of complex **6** (28.6 mg, 0.0268 mmol) and TMB in C_6D_6 was heated at 60 °C. The reaction mixture was stirred for 8 h, after which the ^{1}H NMR spectrum was taken to calculate the percent yield of azoarene produced. To further analyze the product, all solvents were removed under vacuo, and the residue was separated on silica gel using hexanes. The collected orange solution was characterized by mass spectroscopy to confirm the formation of (3,5-$Me_2C_6H_3$)N═N(3,5-$Me_2C_6H_3$).

2.5. Reaction of Tetrazene Complex 6 with 4-methylphenylazide. To a solution of complex **6** (66.2 mg, 0.0621 mmol) in C_6D_6, TMB and azidotoluene (0.2 mL, 0.5 M) in C_6D_6 was added. The reaction was heated at 60 °C for 4 h, upon which a ^{1}H NMR spectrum was taken to show the formation of several azoarenes. To analyze the reaction mixture, all solvents were removed and the crude product was separated on silica gel using hexanes. The obtained orange solution was characterized by mass spectroscopy to show the formation of three different azoarenes.

2.6. ^{57}Fe Mössbauer Spectroscopy. The field- and temperature-dependent Mössbauer spectra were recorded using a spectrometer operated in a constant acceleration mode. The instrument was fitted with a Janis Super-Varitemp, 8DT flow-type cryostat equipped with a superconducting magnet and was cooled using liquid helium. This setup allowed for reaching temperatures between 1.7 and 220 K, as well as for the generation of magnetic fields with a strength of up to 8 T. The field was applied parallel to the propagation direction of the 14.4 keV γ-ray. The light source was incorporated in a vertical velocity transducer system and consisted of a 100 mCi ^{57}Co dispersed in a rhodium foil. The spectra recorded at 4.2 K were obtained, while the sample space of the cryostat was flooded with liquid helium. At higher temperatures, the sample was cooled using a stream of cold helium gas with a flow controlled by a needle-type valve. The sample temperature was determined using a Cernox sensor and was maintained using a 50 Ω heater powered by a Cryocon 32B temperature controller. The isomer shift is reported against the center of the α-iron metal foil spectrum recorded at room temperature.

The spectra were analyzed in the framework of a standard $S = 2$ spin-Hamiltonian, eq 1, as implemented in by the SpinHam option of the WMOSS spectral analysis software (See Co., formerly Web Research Co., Edina, MN).[25]

$$\hat{\mathbf{H}} = \hat{\mathbf{H}}_e + \hat{\mathbf{H}}_n \tag{1}$$

$$\hat{\mathbf{H}}_e = D(\hat{S}_z^2 - 2) + E(\hat{S}_x^2 - \hat{S}_y^2) + \beta_e \hat{\mathbf{S}}\cdot\tilde{\mathbf{g}}\cdot\vec{\mathbf{B}} \tag{2}$$

$$\hat{\mathbf{H}}_n = \delta + \hat{\mathbf{H}}_{\text{Q}} + \hat{\mathbf{S}}\cdot\tilde{\mathbf{A}}\cdot\hat{\mathbf{I}} - \beta_{\text{n}} g_{\text{n}} \hat{\mathbf{I}}\cdot\vec{\mathbf{B}} \tag{3a}$$

$$\hat{\mathbf{H}}_Q = \frac{eQV_{\text{ZZ}}}{12}\left[3\hat{I}_{\text{Z}}^2 - \frac{15}{4} + \eta(\hat{I}_{\text{X}}^2 - \hat{I}_{\text{Y}}^2)\right] \tag{3b}$$

The quantities included in these equations have their conventional meanings. The electric field gradient (EFG) tensor of 3b is described by a set of three principal components, $\{V_{XX}, V_{YY}, V_{ZZ}\}$. In its standard frame, $|V_{ZZ}| \geq |V_{XX}| \geq |V_{YY}|$, the individual EFG tensor components are related to the quadrupole splitting, ΔE_{Q}, and the EFG asymmetry parameter, η, using $\Delta E_{\text{Q}} = (eQV_{ZZ}/2)\sqrt{1 + \eta^2/3}$ and $\eta = (V_{XX} - V_{YY})/V_{ZZ}$. Analysis of the field dependent spectra recorded for **5**−**6** found that the EFG tensor is noncollinear with a zero-field splitting (ZFS) tensor, taken as a reference frame. Consequently, the relative orientation of the EFG tensor with respect to that of the ZFS is described using a set of standard Euler angles $\{\alpha_{\text{EFG}}, \beta_{\text{EFG}}, \gamma_{\text{EFG}}\}$. The observed magnetic hyperfine splitting is quantified by determining the effective magnetic field acting on the ^{57}Fe nuclei. This field results from the vector sum of the applied field and the internal field, $\vec{\mathbf{B}}_{\text{effective}} = \vec{\mathbf{B}}_{\text{applied}} + \vec{\mathbf{B}}_{\text{internal}}$. The internal field is proportional to the field-induced magnetization of the local iron spin, $\vec{\mathbf{B}}_{\text{internal}} = -\langle\hat{\mathbf{S}}\rangle \cdot \tilde{\mathbf{A}}/g_n\beta_n$. At 4.2 K the flip rate of the electronic spin is smaller than the nuclear Larmor precession rate ($1/\tau \leq 10^6$ Hz); that is, the electronic spin is in a slow relaxation regime. For this regime, each individual spin sublevel exhibits an associated Mössbauer spectrum. These subspectra have a magnetic hyperfine splitting determined by $\langle\hat{\mathbf{S}}\rangle\cdot\tilde{\mathbf{A}}$ and an intensity determined by the Boltzmann population of that sublevel. At temperatures higher than 150 K, the spin flip rate becomes larger than 10^9 Hz. Thus, the electronic spin is in a fast relaxation regime for which the simulated spectrum consists of a single spectrum, and the magnetic hyperfine splitting is determined by the thermally averaged spin expectation value $\langle\hat{\mathbf{S}}\rangle_{\text{th}}\cdot\tilde{\mathbf{A}}$.

2.7. HFEPR Spectroscopy. High-field electron paramagnetic resonance (HFEPR) measurements were performed on a transmission-type, home-built spectrometer. The variable-frequency microwaves were generated using a sub-THz wave generator from Virginia Diodes operating at 13 ± 1 GHz and equipped with a cascade of frequency multipliers.[26] The spectrometer was equipped with a 17 T superconducting magnet. The HFEPR spectra were interpreted in terms of the standard $S = 2$ spin Hamiltonian described by eq 2 and were simulated using the program SPIN, written by A. Ozarowski.

2.8. Computational Details. Electronic structure calculations were performed using the Gaussian 09 (revisions A02, C01, and D01) quantum chemical software package.[27] For the computational investigation of the electronic structure and spectroscopy of the tetrazene complex, we used the spin unrestricted formalism, the B3LYP/6-311G functional/basis set combination, and an unabridged structural model.[28] Single point self-consistent field (SCF) calculations and geometry optimizations were completed using standard convergence criteria. The ground state character of a particular electronic configuration was assessed on the basis of time-dependent DFT calculations, that is, all one-electron excitations were found to be positive. The theoretical exchange coupling constants, J, were estimated by comparing the predicted SCF energies of the ferromagnetic (F) and broken-symmetry (BS) states.[29] The initial electronic guesses of the starting SCF calculations were obtained using the default guess option in the case of the F configuration and the *fragment* option of the *guess* keyword for the BS states. While the F state had a septet, $S = 3$ configuration, the BS state corresponds to an $S = 2$ configuration for which 5α, spin-up, electrons are localized on the iron site, while 1β, spin-down, electron was localized on the tetrazene ligand. The value of the exchange coupling constant was obtained using the expression $J = 2(E_F - E_{BS})/5$, where the E_{BS} and E_F energies were obtained from single-point calculations performed either on the X-ray structure or on the geometry optimized structures (using the $\hat{\mathbf{H}} = J\hat{\mathbf{S}}_1 \cdot \hat{\mathbf{S}}_2$ spin Hamiltonian). Spin distributions were assessed based on the Mulliken atomic spin densities. The predicted ΔE_Q and η values describing the electric field gradient and the predicted ^{57}Fe hyperfine coupling constants were estimated using the standard *prop* keyword of the Gaussian code. The predicted isomer shift values were determined using the calibration given by Vrajmasu et al.[30]

Mechanistic investigations were performed using quantum mechanics/molecular mechanics (QM/MM) methods at the ONIOM(OPBE/6-311G(d):UFF) level of theory.[31] Models of both the first (OC(^{t}Bu)$_2$Ph) and second (OC(^{t}Bu)$_2$(3,5-Ph$_2$Ph)) generation alkoxide ligands were studied. The ^{t}Bu and aryl groups of the alkoxide ligand were placed in the MM region. Most geometry optimizations took advantage of the quadratic macrostep option in Gaussian 09.[32] Optimized structures were verified to be minima by analyzing the harmonic frequencies; transition states had a single imaginary frequency corresponding to the molecular motion of that mechanistic step.

3. RESULTS AND DISCUSSION

3.1. Synthesis and Characterization of Fe(OR′)$_2$(THF)$_2$ (2). Synthesis of complex **2** is presented in Figure 2. We have previously reported the two-step preparation of Fe(OR)$_2$(THF)$_2$ (**1**) that involved the reaction of FeCl$_2$ with LiOR to produce Fe$_2$Li$_2$Cl$_2$(OR)$_4$ at the first step;[17b] the latter was then treated with TlPF$_6$ to give Fe(OR)$_2$(THF)$_2$ (**1**).[17c] In contrast, Fe(OR′)$_2$(THF)$_2$ (**2**) is synthesized employing a different, one-step approach, that involves protonolysis of Fe(N(SiMe$_2$)$_2$)(THF)$_x$[24] with 2 equiv of HOR′ (Figure 2). Related reactions of Fe(N(SiMe$_2$)$_2$)(THF)$_x$ with bulky alcohols have been previously reported.[33] Complex **2** is obtained as light-gold crystals isolated in 95% yield by recrystallization from hexanes. X-ray crystal structure of compound **2** (Figure 2) demonstrates a highly distorted tetrahedral geometry with a wide interalkoxide (R′O–Fe–OR′) angle of 141.5(1)°. This value is only slightly larger than the interalkoxide angle of 138.7(1)° in **1**. The magnetic susceptibility value of $\mu_{eff} = 4.7 \pm 0.4\ \mu_B$, obtained for compound **2** by Evans measurements, is consistent with the expected high-spin configuration for the d^6 Fe(II) center in a weak-field ligand environment.

We have also attempted synthesis of "Fe(OR′)$_3$", by treating FeCl$_3$ with 3 equiv of LiOR′. It was previously reported that Fe(OR)$_3$ can be obtained by the reaction of FeCl$_3$ with LiOR; Fe(OR)$_3$ was also obtained as a byproduct of catalysis, along the corresponding azoarenes.[18] In the present case, the reaction of FeCl$_3$ with 3 equiv of LiOR′ (obtained by treatment of HOR′ with n-BuLi) does not lead to the isolation of Fe(OR′)$_3$. We have also synthesized KOR′ and tried to obtain Fe(OR′)$_3$ by treating FeCl$_3$ with KOR′. As in the previous case, no Fe(OR′)$_3$ was isolated. These experiments, along with the fact that Fe(OR′)$_2$(THF)$_2$ can be re-isolated from the nitrene coupling reactions (see below), suggest that the size of [OR′] does not allow formation of stable Fe(OR′)$_3$ species. The increased stability of the catalytically competent bis(alkoxide) form for the bulkier ligand [OR′] led us to postulate that Fe(OR′)$_2$(THF)$_2$ may serve as a better precatalyst for azoarene formation.

3.2. Catalytic Reactivity of 2 in Nitrene Coupling. Our previous report demonstrated that **1** was able to conduct highly efficient formation of azoarenes from aryl azides containing two *ortho* substituents (i.e., mesityl and 2,6-diethylphenyl).[18] In contrast, no reactivity was observed for the less bulky aryl azides (such as 3,5-dimethylphenyl, 2-methylphenyl, or 4-methylphenyl).[18] Complex **2** is also able to efficiently couple mesityl and 2,6-diethylphenyl nitrenes to give the corresponding azoarenes (Table 1) in high yields. As previously observed for **1**, catalysis with **2** proceeds at RT to give azomesitylene and azo(2,6-diethylbenzene) in nearly quantitative yields. More significantly, **2** is also capable of nitrene coupling with other azide precursors, albeit higher catalyst loadings, and heating is required in these cases. Thus, 3,5-dimethylphenylazide forms azo(3,5-dimethylbenzene) in 47% yield after 8 h at 60 °C; heating for 24 h brings the yield of the product to about 70%. Similarly, azoarene formation is observed for aryl azides featuring only one substituent in the *ortho* position (2-Me, 2-Et, 2-^{i}Pr). For example, 2-ethylphenyl azide gives a 65% yield after 8 h. Finally, 4-methylphenyl, 4-trifluoromethylphenyl, or 4-isopropyl azide give comparable yields of 16%, 15%, and 14%, respectively (approximately one turnover), after 8 h at 60 °C; longer heating (24 h) improves the azoarene yield for 4-methylphenyl azide to 33%. In contrast, longer heating times do not improve the yields of 4-

Table 1. Complex 2-Catalyzed Formation of Azoarenes from the Corresponding Azides

entry	azide	catalytic loading (mol %)	time (h)	temperature (°C)	yield[a] (%)
1	MesN$_3$	5	4	25	100
2	2,6-Et$_2$PhN$_3$	5	24	25	100
3	3,5-Me$_2$PhN$_3$	10	8	60	40
4	3,5-Me$_2$PhN$_3$	10	24	60	69
5	2-MePhN$_3$	10	24	60	47
6	2-EtPhN$_3$	10	8	60	65
7	2-^{i}PrPhN$_3$	10	8	60	53
8	2-PhPhN$_3$	10	24	60	15
9	2-OMePhN$_3$	10	24	60	14
10	4-^{i}PrPhN$_3$	10	8	60	15[b]
11	4-MePhN$_3$	10	8	60	16
12	4-MePhN$_3$	10	24	60	33
13	4-CF$_3$PhN$_3$	10	8	60	14[b]
14	4-OMePhN$_3$	10	8	60[a]/100[c]	0

[a]The reactions were conducted in C$_6$D$_6$ in the presence of an internal standard (trimethoxybenzene or hexamethylbenzene), and the yields were determined by ^{1}H NMR spectroscopy. GCMS yields were similar and are given in the Supporting Information. [b]Longer heating of these samples produced insoluble materials; no yield improvement was observed by ^{1}H NMR spectroscopy. [c]The reaction at 100 °C was conducted in C$_7$D$_8$ in the presence of an internal standard.

DOI: 10.1021/acs.inorgchem.8b01418
Inorg. Chem. 2018, 57, 9425−9438

trifluoromethylphenyl or 4-isopropylphenyl azides, producing instead a black insoluble material, which we were unable to identify. No product formation was observed for 4-methoxyphenyl azide.

3.3. Synthesis and Characterization of Iron Tetrazene Complexes (3−6). As the catalytic reactivity of complex **2** with some aryl azides differs significantly from that of **1**, we became interested in the interrogation of the reaction mechanism. To gain an initial insight, we investigated stoichiometric reactivity of complex **2** with bulky and nonbulky aryl azides. Treatment of the pale-yellow solution of **2** with 2 equiv of mesityl azide or 2,6-diethylphenyl azide leads to N_2 evolution and a color change to red-brown. ^1H NMR spectroscopy indicates nearly quantitative formation of the corresponding azoarene products. These results are consistent with the results previously obtained for **1**.[18] In contrast to compound **1**, however, compound **2** does not lead to the formation of the iron tris(alkoxide) complex $Fe(OR')_3$ as a byproduct of nitrene coupling. Following mesityl nitrene coupling, we were able to re-isolate compound **2**. We were not able to determine its yield as it cocrystallizes with the azomesitylene.

The reaction of **2** with nonbulky aryl azides takes a different route from that of compound **1** (Figure 1). Treatment of **2** with 2 equiv of aryl azides N_3Ar lacking *ortho* substituents (azidobenzene, 4-azidotoluene, 4-azidoanisole, 3,5-dimethylphenyl azide) leads to the formation of deep-green solutions. Recrystallization of the crude products from ether or hexanes solutions leads to the isolation of dark-green tetrazene complexes **3−6** (Figure 3). Compounds **3−6** were characterized by elemental analysis, solution magnetic measurements, and IR spectroscopy. Selected compounds were also characterized by X-ray crystallography, field-dependent ^{57}Fe Mössbauer spectroscopy, and high-field electron paramagnetic resonance (HFEPR) (*vide infra*).

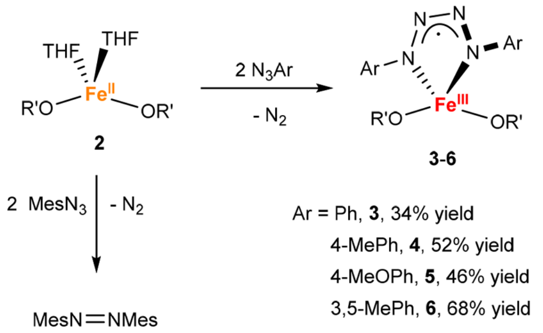

Figure 3. Stoichiometric reactivity of azides with **2**: synthesis of $Fe(OR')_2(ArNNNNAr)$ complexes **3−6** vs nitrene coupling for the bulkier mesityl azide.

The structures of compounds **3** and **5** are given in Figure 4. These structures confirm the coordination of the 1,4-tetrazene ligand to yield a distorted tetrahedral iron center. Due to the lower quality of the structure of **3**, only the metric parameters of **5** are discussed in detail. However, metric parameters for **3** follow the trends described for **5** and can be found in the corresponding CIF deposited with the CCDC. The iron-alkoxide bond distances in **5** are shorter than the corresponding distances in **2** (1.792(1)/1.795(1) Å vs 1.828(2)/1.854(2) Å), suggesting a higher oxidation state of Fe in **5**. The iron-1,4-tetrazene chelate is planar, with flanking anisole groups displaying different torsion angles of 14 and 31 deg. The structure is nearly C_2-symmetric, albeit C_2 symmetry is not observed crystallographically due to the different torsion angles of the anisole groups. The bond distances in the 1,4-tetrazene fragment indicate that N1−N2 and N3−N4 distances of 1.322(2) and 1.316(2) Å are similar to the N2−N3 distance of 1.325(2) Å, all being intermediate between N−N and N═N bonds.[34] The redox-active nature of metal-bound tetrazene, that is capable of adopting three different oxidation states (2−/1−/0), has been previously discussed by Holland and co-workers,[35,36] and Riordan and co-workers.[37] The similarity in the tetrazene N−N bond distances in **5** suggests that the tetrazene ligand is in the radical anion (1−) state, which indicates an Fe(III) center (see below for ^{57}Fe Mössbauer and HFEPR discussion). Other reported iron tetrazene complexes include the Fe(II)-tetrazene radical anion reported by Holland and Riordan,[35−37] the Fe(IV)-tetrazene dianion reported by Jenkins and co-workers,[38] and the pyridine(diimine)-supported Fe(III)/Fe(II)-tetrazene dianion/monoanionic radical complexes very recently reported by Chirik and co-workers.[39]

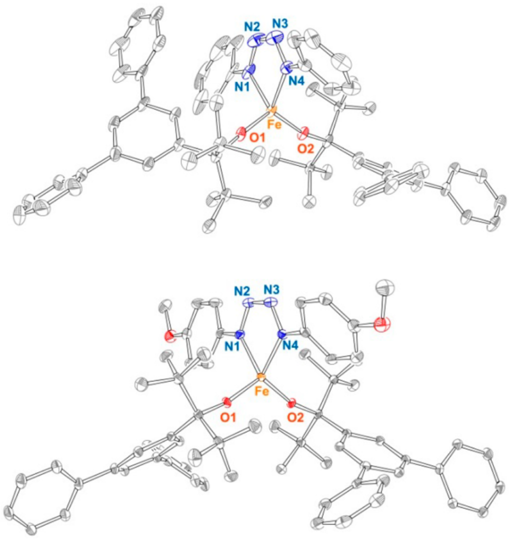

Figure 4. Top: X-ray structure of **3**, 30% probability ellipsoids. Bottom: X-ray structure of **5**, 50% probability ellipsoids. Selected bond distance (Å) and bond angles (°) for complex **5**: Fe O1 1.792(1), Fe O2 1.795(1), Fe N4 2.010(1), Fe N1 2.023(1), N1 N2 1.322(2), N3 N2 1.316(2), N3 N4 1.325(2), O1 Fe1 O2 115.03(5), N4 Fe1 N1 75.67(5).

3.4. HFEPR Spectroscopy. To determine the electronic structure of the tetrazene-containing iron complexes, we have performed a combined field-dependent ^{57}Fe Mössbauer and high-frequency (HF) EPR spectroscopic investigation of **5** and **6**. These studies demonstrate that **5−6** exhibit a quintet $S = 2$ ground-spin state, *vide infra*. Although these compounds are obtained by reacting high-spin ferrous ions with neutral ligands, this investigation shows that the resulting quintet ground state configuration of **5−6** does not originate from the presence of an iron(II) site but rather from the presence of a high-spin ferric ion ($S = 5/2$) and a paramagnetic ligand. Thus, the tetrazene ligand is redox noninnocent exhibiting a $S = 1/2$ that is antiferromagnetically coupled to the $S = 5/2$ of the iron(III) ion.

Inspection of Figures S8.1 and S10.1 shows that for these two compounds the spectra recorded for neat powders are

DOI: 10.1021/acs.inorgchem.8b01418
Inorg. Chem. 2018, 57, 9425−9438

essentially identical. Consequently, we assume that these complexes are describable by the same set of fine and hyperfine structure parameters. In this section, we present spectra obtained for **6**. The HFEPR spectra of **6** were recorded at frequencies ranging from 48 to 610 GHz. Some of these spectra are shown in Figures 5, S10.2, and S10.3. These spectra are information-rich, and we observed many resonances that could be associated with **6** at each frequency, allowing us to build up a detailed plot of the frequency vs field dependence of the observed resonances, see Figure 6.

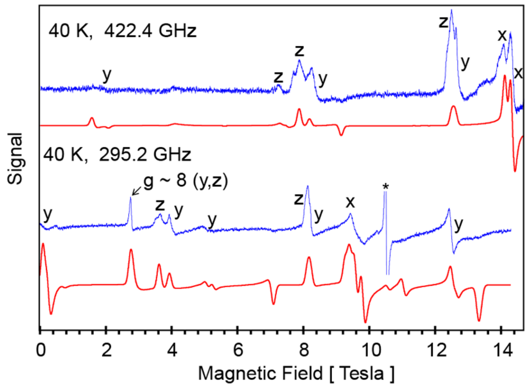

Figure 5. Shown in blue are HFEPR spectra recorded for **6** at 40 K, 422.4 GHz (top) and 295.2 GHz (bottom). The solid red lines are simulations obtained using the $S = 2$ spin-Hamiltonian of eq 2 and the parameters listed in Table 2. The resonance labeled using the (*) symbol appears at $g = 2.003$ and is generated by a radical-type, minute impurity. The *x*, *y*, *z* labels of the experimental spectra highlight the nature of the respective canonical resonance.

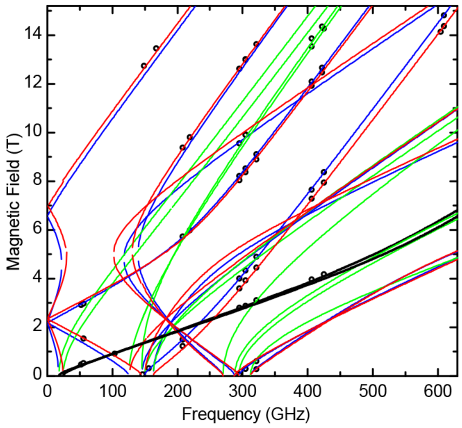

Figure 6. Field- vs frequency-dependence of the observed resonances (black dots). The red, blue, and green traces show the theoretical dependence of the *z*, *y*, and *x* canonical resonances calculated using eq 2 and the parameters listed in Table 2. The two black lines highlight the $g \approx 8$ resonances at *y* and *z* orientation.

The entire set of spectra and the frequency vs field dependence of the observed resonances were analyzed in the framework of the standard $S = 2$ spin-Hamiltonian described by eq 2. Our initial analysis of the field-dependent Mössbauer spectra revealed a quintet ground spin state with a small ZFS described by a positive $D \approx +2(1)$ cm^{-1}. However, inspection of the low-temperature spectra revealed a relatively strong $g \approx 8$ resonance; see Figure S10.2. Typically, for an $S = 2$ spin system, such a resonance is associated with an apparent $\Delta m = 4$ transition between the nominal levels $M_S = 2$ and $M_S = -2$, and, usually, is indicative of a negative ZFS parameter D, since the $M_S = -2$ level is a ground state in such situation. Therefore, to assess whether this resonance does indeed originate from a $|S, m\rangle \approx |2, \pm 2\rangle$ ground quasi-doublet, we have considered its temperature-dependent behavior; see Figure S10.4. These spectra clearly showed that this resonance did not follow a dependence expected for either a ground- or an excited-state resonance. Inspection of Figure S9.1 revealed the origin of this puzzling observation. Thus, for $E/D \approx 0$ and $D < 0$, in zero-field, the five spin-sublevels are organized into two sets of quasi-doublets and a singlet, the later having the highest energy. In contrast, for $E/D \approx 1/3$, such as in the case for **6**, we observe only singlets, and the spin-sublevels are symmetrically distributed around the middle (the third) spin sublevel. Furthermore, the magnetic properties of the lowest and highest quasi-doublets are virtually identical except that while one quasi-doublet magnetizes along the *y* direction the other magnetizes along *z*. In such a case, a $g \approx 8$ resonance is expected for transitions between both the two highest and the two lowest sets of spin sublevels. These observations suggest that for **6** the $g \approx 8$ spectral feature originates not from a single resonance but rather from the overlap of two distinct, *y*- and *z*-type canonical resonances. Since D is small, the excited resonance is observed even at the lowest temperature for which we have recorded spectra, that is, 5 K. If D were large (and $E \approx D/3$), the $g \approx 8$ resonance would still be observed, either at the canonical Z or Y orientation, depending on the sign of D.

As it is typically done in this laboratory, the spin Hamiltonian parameters were determined by fitting the frequency dependencies shown in Figure 6. Inspection of Figures 4 and 5 reveals two sets of resonances that occur near zero magnetic field for spectra recorded at frequencies ~150 GHz and ~300 GHz. This observation indicates that E must indeed be close to $D/3$. In the case of a small E/D ratio, the zero-field frequencies should obey the ratios 1:3:4.

Finally, some of our simulations of the 5 K spectra suggest that for this complex the E/D parameter is distributed such that $\sigma(E/D) \approx 0.04$ and $(E/D)_o = 0.33$; see Figure S10.5. While such a distribution is not unusual, what makes it peculiar in this case is that it is centered on an E/D value of 1/3. This leads for $E/D > 1/3$ to a change in the sign of D and to a reorientation of the standard frame of the ZFS tensor; see Table S2. These spin-Hamiltonian parameters, small D and the g component values close to 2 are inconsistent with an $S = 2$ state originating from a Fe^{2+} or a Fe^{4+} system, but are consistent with the presence of a high-spin ferric ion (see the Mössbauer section below).

3.5. Field-Dependent ^{57}Fe Mössbauer Spectroscopy.

The zero-field spectra of **6** exhibit a well-defined quadrupole doublet, which at 4.2 K, is described by an isomer shift $\delta = 0.495(5)$ mm/s, a quadrupole splitting $\Delta E_Q = 2.201(4)$, and line width $\Gamma = 0.33(1)$ mm/s. For the sample shown here, the doublet accounts for ~85% iron present in the sample. The remaining iron amount is associated with an EPR-silent species that exhibits a broad magnetic hyperfine splitting pattern that is typically associated with heterogeneous iron(III) nanoparticles. Inspection of Figure S8.2 and Table S4 shows that for these compounds the quadrupole splitting is essentially temperature independent and that the isomer shift exhibits only a slight decrease in its value such that at 180 K $\Delta E_Q = 2.16(1)$ and $\delta = 0.43(1)$ mm/s. The change of the latter parameter is attributed to a typical second-order Doppler shift. Furthermore, as the temperature is increased, the observed spectra exhibit a higher than expected decrease in their intensities due to an accentuated decrease in the recoilless fraction of ^{57}Fe nuclei, see Figure S8.2. The observed isomer shift value is typical of high-spin iron(III) ions. Moreover, the presence in this case of a high-spin Fe^{3+} ion is further corroborated by inspection of Table 3, which shows that this value is considerably different from both those observed for the tetrazene-supported high-spin Fe(II/I) complexes of Holland[35,36] and for the low-spin Fe(IV/III) compounds of Jenkins,[38] but that they are similar to those determined for the high-spin Fe(III) of Chirik.[35,39]

The observation at 4.2 K of a quadrupole doublet suggests that **6** is a non-Kramers system, that is, it has an integer spin. This observation together with the HFEPR spectra and the room-temperature value of the magnetic moment indicate the presence of an $S = 2$ ground state. Inspection of Figure 7 shows that even a relatively small field of 0.5 T induces a large magnetic hyperfine splitting. This behavior demonstrates that at 4.2 K the electronic spin is in a slow relaxation regime (a spin flip rate <10^6 Hz). Moreover, at 4.2 K the maximal field-induced hyperfine splitting is observed below 1 T followed by a slight decrease at higher fields. While the central portion of the 0.5−1.0 T spectra accounts for most of the spectral area, for the 4−8 T spectra the two outermost resonances spectral features have the highest area. Together, these observations suggest that the zero-field splitting (ZFS) of the quintet ground state of **6** is sufficiently small that, at least along one spatial direction, it is easily overcome by a small ($B < 1$ T) applied field. Moreover, the distinct difference between the shapes of the low- and high-field, 4.2 K spectra shows that as the strength of the magnetic field increases it leads to a gradual depopulation of several spin-sublevels, suggesting a positive D value. These inferences are corroborated by our simulations. Thus, the solid red lines of Figure 7 are theoretical curves obtained using the standard $S = 2$ spin-Hamiltonian of eq 1 assuming a relatively small and rhombic ZFS tensor; that is, $D = 2.31$ cm^{-1} and $E/D = 0.25$. These values were substantiated by the analysis of the HFEPR spectra, *vide supra*. Inspection of Figure S9.1 shows that for fields below 2 T these parameters lead to a nearly uniaxial set of spin expectation values for the lowest spin sublevel, $|\langle\hat{S}_y\rangle| \gg |\langle\hat{S}_x\rangle| \approx |\langle\hat{S}_y\rangle| \approx 0$. Since for $B \approx 0.5$ T the $\langle\hat{S}_y\rangle$ of the ground-spin sublevel saturates to a value of −2 the extent of observed hyperfine splitting is determined by $B_{\mathrm{int},y} = -\langle\hat{S}_y\rangle A_y/g_n\beta_n$. Consequently at 4.2 K the $B \leq 3$ T spectra are virtually independent of $A_{x,z}$ and are essentially determined by A_y. While A_x begins having a stronger influence at higher fields, even at 8 T our simulations are insensitive to A_z. This behavior is easily understood when the spin-expectation values and Boltzmann populations of the two lowest spin sublevels are considered; see Figure S9.1. Unlike for y, a magnetic field applied along x leads to a sizable $\langle\hat{S}_x\rangle$ spin expectation value only above 2 T. In contrast, a field applied along z fails to separate the two lowest spin sublevels. This leads to considerably lower $B_{\mathrm{int},z}$ values and comparable Boltzmann populations for these two spin-sublevels. Unfortunately, this behavior severely limits the precision with which A_x and A_z can be determined, see Table 2. In principle these values can be further refined by considering spectra recorded at higher temperatures. However, in this case, our efforts were impeded by the low resolution of the 150−180 K spectra, due to the low recoilless f factor observed at high-temperatures, and by the presence for the 10−100 K spectra of an intermediate relaxation regime of the electronic spin, see Figure S8.3. Inspection of Figure S9.2 shows that for $T > 100$ K, we expect a Curie-like regime, $\langle\hat{S}\rangle_{\mathrm{th}} \approx 1/T$. For these conditions the observed magnetic hyperfine splitting is essentially determined by the nuclear Zeeman interaction being minimally influenced by the ZFS. This behavior allowed us to assess the rhombicity of the EFG tensor, yielding a moderate $\eta = 0.5(2)$ EFG

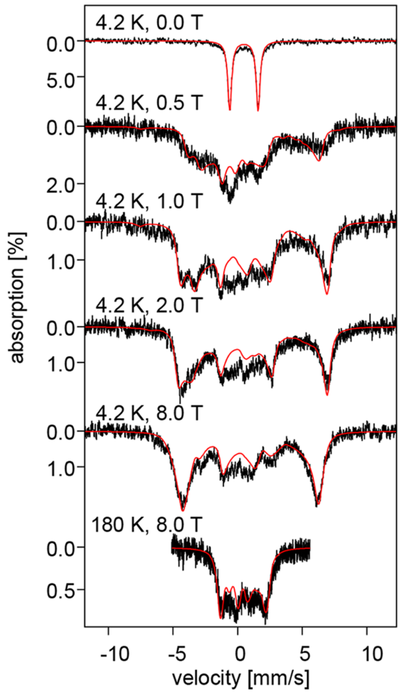

Figure 7. Field- and temperature-dependent ^{57}Fe Mössbauer spectra recorded for a neat powder sample of **6**. The solid red lines are simulations obtained using eq 1 and the parameters listed in Table 2.

Table 2. Fine and Hyperfine Structure Parameters of the Tetrazene-Supported Iron(III) Complexes

S	δ [mm/s]	ΔE_Q[a] [mm/s]	η[a]	D[b,e] [cm^{-1}]	E[f]	g_x[b]	g_y[b]	g_z[b]	$A_x/g_n\beta_n$[d] [T]	$A_y/g_n\beta_n$[d] [T]	$A_z/g_n\beta_n$[d] [T]	$A_{iso}/g_n\beta_n$[c,d]
2	0.49(1)	2.15(5)	0.5(2)	2.31(1)	0.71(1)	2.013(6)	1.999(3)	2.006(6)	−17(2)	−19.2(4)	−20(5)	−19(3)

[a] The EFG tensor is rotated from the reference frame (ZFS tensor orientation) by $\alpha_{\mathrm{EFG}} = 76(9)°$, $\beta_{\mathrm{EFG}} = 90°$, $\gamma_{\mathrm{EFG}} = 20(10)°$. [b] Values determined from HFEPR. [c] For the $I = 1/2$ ground state of the ^{57}Fe nuclei, this value corresponds to ∼ −26(4) MHz (1 T = 1.381 MHz). [d] These are effective hyperfine splitting values obtained for the $S_t = 2$ ground state. The values intrinsic to the high-spin Fe(III) site can be obtained using $A(S_{\mathrm{Fe(III)}} = 5/2) = 6 \cdot A(S_t = 2)/7$ which, for A_{iso} leads to ∼ −16 T. [e] This is an effective value obtained for the $S_t = 2$ ground state. The intrinsic value is obtained using $D(S = 2) = \frac{8}{6}D(S_{\mathrm{Fe}} = 5/2)$ which yields $D(S_{\mathrm{Fe(III)}} = 5/2) = 1.73$ cm^{-1}. [f] This value was determined from HFEPR. However, the simulations of the field-dependent Mössbauer spectra of Figure 7 were obtained using $E/D = 0.25$.

DOI: 10.1021/acs.inorgchem.8b01418
Inorg. Chem. 2018, 57, 9425−9438

Table 3. Predicted and Experimental Zero Field Mössbauer Parameters of **5** and Other Selected Iron Tetrazene Complexes

complex/model		formal charge (spin)		S	δ [mm/s]	ΔE_Q [mm/s]	ref
		Fe	N_4R_2				
5	expt.	+3 (5/2)	−1 (1/2)	2	0.49(1)	2.20(1)	current work
	calcd. F				0.43	1.91	
	calcd. BS				0.43	2.06	
$L^{Me}Fe(Ad_2N_4)$	expt.	+2 (2)	−1 (1/2)	3/2	0.69(2)	1.32(4)	35
	calcd.				0.65	2.04	
$[L^{Me}Fe(Ad_2N_4)][K(crypt\text{-}222)]$	expt.	+2 (2)	−2 (0)	2	0.81(2)	1.40(2)	
	calcd.				0.72	*>4.0*	
$[L^{CF3,Cl}Fe_1(Ad_2N_4)Fe_2L^{CF3,Cl}]$	Fe_1	+2 (2)	−1 (1/2)	n.a.	0.73(2)	1.45(2)	36
	Fe_2	+1 (3/2)			1.21(2)	2.08(2)	
$[L^{CF3,Cl}Fe(N_4Ad_2)]$		+2 (2)	−1 (1/2)		0.75(4)	1.55(6)	
$[(^{Me,Et}TC^{Ph})Fe(p\text{-}tolyl_2N_4)](PF_6)_2$		+4 (0)	−2 (0)	0	−0.01	0.62	38
$[(^{Me,Et}TC^{Ph})Fe(p\text{-}tolyl_2N_4)](PF_6)$		+3 (1/2)	−2 (0)	1/2	0.10	1.13	
$(^{iPr}PDI)Fe[NN(N\text{-}^1Ad)]$[a]		+3 (5/2)	−2 (0)	2	0.57	3.10	39
$(^{iPr}PDI)Fe[NN(N\text{-}SiMe_3)_2]$[a,b]		+3 (3/2[c])	−2 (0)	1	0.42[c]	1.32[c]	
		+3 (5/2[d])	−2 (0)	2	0.53[d]	3.26[d]	
$(^{iPr}PDI)Fe[NN(N\text{-}3,5\text{-}Me_2C_6H_3)_2]$[a]		+3 (3/2)	−2 (0)	1	0.43	1.37	
$(^{iPr}PDI)Fe[NN(N\text{-}Bn)_2]$[a]		+2 (1)	−1 (1/2)	0	0.23	2.99	
$(^{iPr}PDI)Fe[NN(N\text{-}^cOct)]$[a]		+2 (1)	−1 (1/2)	0	0.28	2.98	

[a] The pyridine(diimine) ligand, ^{iPr}PDI, is monoanionic and exhibits an $S = 1/2$ ground state. [b] This compound exhibits spin crossover behavior. [c] Major component at low temperatures ($T < 120$ K). [d] Major component at high temperatures ($T > 150$ K).

asymmetry parameter. Interestingly, the combined analysis of the high temperature and 4.2 K, field-dependent spectra showed that the standard frame of the EFG tensor, for which $|V_{ZZ}| \geq |V_{XX}| \geq |V_{YY}|$, is rotated from that of the ZFS tensor such that the large positive component of the EFG is roughly aligned with $B_{int,y}$. Consequently, the expression of the EFG tensor in its proper frame ($0 \leq \eta \leq 1$) required the introduction of a standard set of Euler angles to describe its orientation with respect to the orientation of the ZFS tensor taken as the reference frame. Knowledge of the relative orientation of the ZFS, $\tilde{\mathbf{g}}$, and EFG tensors allows us to infer, experimentally, the relative orientation of the magnetization vector with respect to distribution of the atomic charges of **5**–**6**. Finally, the values presented in Table 2 represent our best estimates, including the errors, of the fine and hyperfine structure parameters obtained from a large series of simulations and fits of the entire set of spectra.

3.6. Ground-State Electronic Configuration of the Iron-tetrazene Complexes.

To gain insight into the electronic structures and the origin of the observed spectroscopic parameters of these complexes, we have performed a series of DFT calculations. In this study we used an unabridged structural model of **5** and the B3LYP/6-311G functional/basis set combination. This investigation revealed that the predicted ground state of **5** is of a broken-symmetry (BS) type for which nearly five α electrons are localized on the iron ion and one β electron is delocalized on the tetrazene ligand, see Figure 8. Interestingly, inspection of Table 3 shows that the predicted zero-field Mössbauer parameters of **5** are in very good agreement with those observed experimentally. Consequently, these calculations suggest that the ground state originates from the strong antiferromagnetic coupling of a $S = 5/2$ spin of a high-spin iron(III) site with that of a $S = 1/2$ tetrazene-based spin. To evaluate the strength of the exchange interaction between the two spins, we have compared the predicted properties and the self-consistent field (SCF) energies of the BS and of the corresponding ferromagnetic (F) state. For the F state all six unpaired electrons have the same α spin. As expected, we found that the zero-field Mössbauer parameters, the charge, and spin distributions predicted for the F state are nearly identical to those obtained for the BS state. However, the SCF energy of the F state is ~2000 cm^{-1} higher than that of the BS state in the case of calculations performed on the X-ray structure and ~1180 cm^{-1} for the geometry optimized structures. These energies suggest that $J = 941$ cm^{-1} for the nonoptimized and $J = 550$ cm^{-1} for the optimized structures (Table S7), respectively (using the $J\hat{\mathbf{S}}_1 \cdot \hat{\mathbf{S}}_2$ formalism).

The combined analysis of the field-dependent Mössbauer and HFEPR spectra recorded for **5** revealed a quintet ground spin state characterized by a small ZFS and a nearly isotropic g tensor for which $g_{iso} \approx g_e = 2.00$. These parameters point to an essentially fully quenched angular orbital momentum and to the presence for this complex of an isolated orbital state. In particular, the D value of **5** is considerably smaller than that expected for high-spin configurations of iron ions that have high-spin, $S = 2$ ground states, that is, iron(IV) ($D \approx +10$ cm^{-1}) and iron(II) ($|D| = 5$–20 cm^{-1}).[40] Moreover, the $D_t = 2.29$ cm^{-1} of the $S_t = 2$ of **5** ($\overrightarrow{\mathbf{S}}_{t} = \overrightarrow{\mathbf{S}}_{Fe} + \overrightarrow{\mathbf{S}}_{ligand}$), obtained from the antiferromagnetic coupling of a $S_{Fe} = 5/2$ with a $S_{ligand} = 1/2$ tetrazene-based spin, when the proper spin-coupling coefficient are considered, $D(S_t = 2) = \frac{8}{6}D(S_{Fe} = 5/2)$, yields $D(S_{Fe} = 5/2) = 1.71$ cm^{-1}. This value is well within the range of values observed for high-spin iron(III) sites. This much smaller ZFS originates from the presence for **5** of an iron(III) site with a half-filled valence shell that leads to an isolated $^6A_1$ singlet orbital ground state. This assignment is further corroborated by the isomer shift value which is typical of ferric ions with a sextet spin state. The g values are also a good indication of an Fe^{3+}, as larger values would be expected for Fe^{2+} even when coupled to a radical. However, for such a state, the spherically symmetric charge distribution engendered by the half-filled shell should also lead to a vanishing EFG tensor and thus to a null quadrupole splitting. This expectation

DOI: 10.1021/acs.inorgchem.8b01418

is in stark contrast to the observed experimental value (ΔE_{Qexpt} = 2.20 mm/s), which, however, is well reproduced by our calculations ($\Delta E_{Qcalc, BS}$ = 2.06 mm/s).

Thus, inspection of Figure 7 shows that the largest component of the predicted EFG tensor is positive and is found orthogonal to the OFeO plane defined by the two alkoxo ligands. When the EFG produced by the two large, negative atomic charges of the two oxygen atoms are considered, this observation suggests that the observed EFG tensor is dominated not by the 3d valence electrons of the iron(III) ion but rather that generated by the ligand charges. This effect is well reproduced by our DFT calculations, see Table S6. In other words, the magnitude of the quadrupole splitting is determined by the ligand contribution to the EFG tensor. The observation of a large quadrupole splitting for a high-spin iron(III) complex is not unprecedented. Two notable examples are the large quadrupole splitting of some Fe(III)-porphyrins (ΔE_Q = +1 to +2 mm/s)[41] and of $Fe^{III}[N(SiMe_3)_2]_3$ (ΔE_Q = +5.12 mm/s).[42]

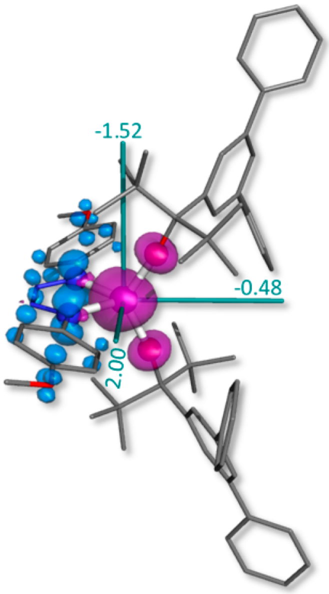

Figure 8. Unpaired spin density plot calculated for the geometry optimized structure of the BS state of **5** at the B3LYP/6-311G level of theory. The alpha spin density is shown in purple, the beta spin density is shown in blue, and the plot was obtained using an isosurface value of 0.006 e/Bohr^3. The axes shown in green indicate the orientation of the predicted EFG tensor. The numerical values indicate the magnitude of the respective tensor components expressed in mm/s. The experimental values are 2.07 mm/s, −1.55 mm/s, and −0.52 mm/s; see Table S6.

3.7. Mechanistic Studies.

It is generally accepted that tetrazenes are formed by the [2 + 3] cycloaddition of metal-nitrene complex with an organoazide.[34,43,44] In our case, this assumption indicates that the "Fe(OR′)$_2$" system first forms a Fe(OR′)$_2$(NAr) (nitrene) complex. What is the role of 1,4-tetrazene species in the formation of azoarenes in Fe(OR′)$_2$ system? One could propose three possible roles of tetrazene: (1) an obligatory reaction intermediate to the azoarenes; (2) a "masked form" of reactive iron-nitrene species, whose formation is reversible, and which may not directly lead to azoarenes, but which may enable their formation by reforming reactive nitrene or some other species; (3) a side product that is not relevant to the main reaction path that leads to the azoarenes, and whose formation is irreversible. We note that Jenkins and co-workers have recently demonstrated that in their tetracarbene (TC) system, Fe(TC)(ArNNNNAr) complex forms azoarene upon heating; it also forms aziridines upon reaction with olefins (Figure 9a).[40] Zdilla and co-workers have demonstrated that the formation of Mn-tetrazene in Mn(ArNNNNAr)$_2$ was reversible and detected the ring-opened Mn-imido-azide intermediate (Figure 9b).[45] Hillhouse and Cundari proposed that formation of azoarenes takes place via a 1,2-tetrazene in nickel-diphosphine system (Figure 9c).[13] Finally, Peters and co-workers have investigated the mechanism of catalytic formation of azoarenes in their iron and ruthenium systems, and found no evidence for tetrazene participation. Instead, mechanistic evidence pointed to the direct nitrene coupling for ruthenium, and for metal-imido coupling for iron (Figure 9d).[14]

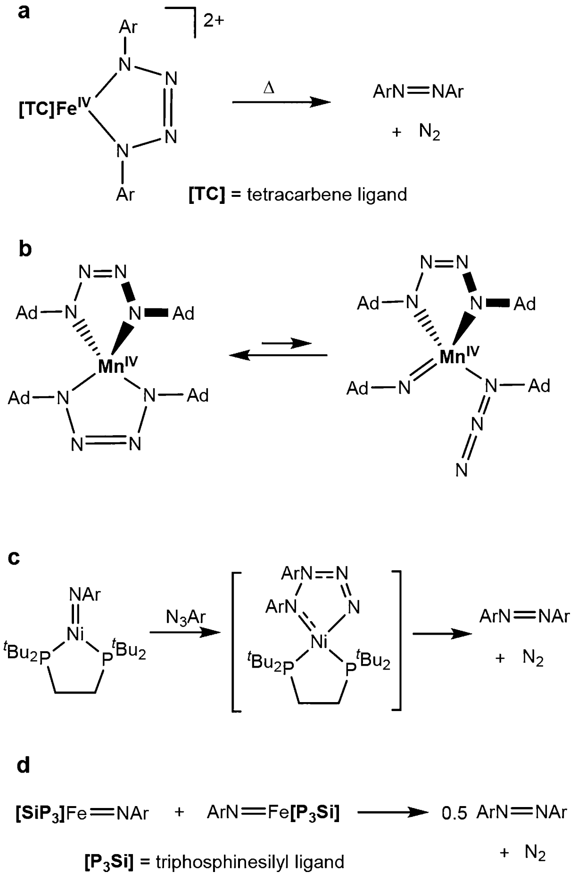

Figure 9. Previously reported reactions of metal-imido of relevance to tetrazene or azoarene chemistry.[13,14,40,45]

To shed light on the role of 1,4-tetrazene in our system, we interrogated whether the Fe(OR)$_2$(ArNNNNAr) complexes can form azoarenes. We specifically focused on the reactivity of complexes **4** or **6**, as they can be isolated in a relatively good yield. Heating C_6D_6 solution of **4** or **6** to 50 °C for 8 h produces the corresponding azoarene. The formation of aroarene was also confirmed by mass spectrometry. Treatment of complex **6** with the C_6D_6 solution of azidotoluene results in the formation of three different azoarenes, two symmetric and one asymmetric (Figure 10), as confirmed by mass spectrometry (Supporting Information). These experiments

DOI: 10.1021/acs.inorgchem.8b01418
Inorg. Chem. 2018, 57, 9425−9438

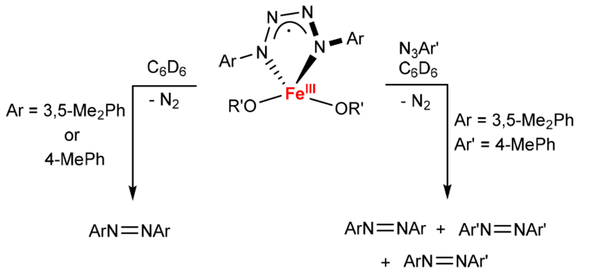

Figure 10. Stoichiometric reactions of tetrazene complexes forming azoarenes.

suggest that while (i) tetrazenes are relevant to the catalytic cycle that produces azoarenes, (ii) they appear to be in equilibrium with an iron mono(imido) species that can, upon reaction with a different azide, form a mixed azoarene product. For further insight into the reaction mechanism, we turned to computational exploration of the potential energy surface.

QM/MM calculations were employed to probe the reaction mechanism of tetrazene and azoarene formation.[32] Although these results employ the less sterically bulky first-generation alkoxide ligand ($\mathrm{OC(^tBu)_2Ph}$), this choice allowed for a more complete data set to be obtained. The thermodynamics of the full model (see Supporting Information) are nearly identical, suggesting that the conclusions reached for this small model are also valid for the experimental system. Multiple rotational conformations within the alkoxide arms were probed for each species/spin state. Typically, these rotamers fell within 3−5 kcal/mol of the lowest energy rotamer (Table S9). Only the lowest energy spin state and rotamer are reported in the manuscript. The 4-methoxyphenyl azide substrate was used for all calculations.

Figure 11 (left) shows the optimized structure of the lowest energy iron mono(imido) complex (**i**). This quintet was calculated to be nearly isoenergetic with the triplet imido complex (ΔG = 0.7 kcal/mol). The tetrazene (**ii**) favors the quintet (Figure 11 middle) that was calculated to be 12.6 and 3.3 kcal/mol lower in energy than the triplet and septet tetrazenes, respectively, consistent with spectroscopy and full model DFT calculations. The transition state for tetrazene formation (**i**−**ii**−**TS**, Figure 11 right) has a barrier of 20.9 kcal/mol leading to **ii** that is −8.5 kcal/mol relative to free azide and **i**. This transition state is consistent with 1,3-dipolar addition of the azide to **i**. The exergonic formation of **ii** is consistent with isolation of the tetrazene, yet the reverse barrier of 29.4 kcal/mol is accessible, meaning that under appropriate conditions, and assuming that azoarene formation directly from **i** does not have a lower barrier, then the tetrazene may act as a masked iron mono(imido) complex similar to the Mn complex reported by Zdilla and co-workers.[45]

Next, we explored how azoarene can form: (i) through formation of the 1,2-tetrazene proposed by Hillhouse and Cundari,[13] (ii) directly from **ii** through N$_2$ loss, (iii) from **i** and azide with N$_2$ loss, and (iv) by dimerization of two equivalents of **i**.[14] The 1,2-tetrazene was found to be endergonic by 19.4 kcal/mol vs **ii** (and 10.9 kcal/mol higher in energy than free azide and **i**). Moreover, its barrier is 9.4 kcal/mol higher than **i**−**ii**−**TS**, meaning that it is neither kinetically nor thermodynamically competitive allowing us to rule out pathway (i). N$_2$ loss from **ii** to form a quintet bis(imido) complex **iii**, Figure 12 (left), is found to be slightly endergonic relative to **ii** by 5.2 kcal/mol, but with a prohibitive barrier of 45.3 kcal/mol for **ii**−**iii**−**TS** (Figure 12 middle). Coupling of the imidos in this putative intermediate to form the azoarene complex **iv** is quite exergonic at −43.7 kcal/mol vs **iii**, and with a reasonable barrier of 3.0 kcal/mol. Thus, if the bis(imido) species can be formed, then azoarene formation should proceed smoothly, but pathway (ii) is not kinetically feasible on the quintet surface. The formation of **iii** directly from **i** and azide was also found to have a prohibitive barrier of 40.7 kcal/mol (**i**−**iii**−**TS**, Figure 12 right), ruling out pathway (iii). Calculation of alternative spin states for the bis(imido) complex demonstrated that the triplet is favored over the quintet by 10.5 kcal/mol. Unfortunately, formation of this intermediate from the triplet form of **ii** or **i** and azide is found to have a barrier of 35.1 and 41.2 kcal/mol, respectively, ruling out pathways (ii) and (iii) on the triplet surface as well. Not only are all of these barriers higher than the reverse barrier to azide and **i** from the tetrazene, but these barrier heights are also inconsistent with the experimental conditions. Finally, dimerization of **i** to form a bridging azoarene between 2 equiv of Fe(OR)$_2$ (**v**) was probed on the nonet surface. A reasonable barrier of 19.8 kcal/mol is calculated, and the reaction is exergonic by −21.6 kcal/mol. Therefore, pathway (iv) is predicted to be the most feasible pathway for azoarene formation.

Figure 13 summarizes all of these thermodynamics for both the quintet and triplet surfaces. This potential energy surface suggests that azoarene and tetrazene formation are kinetically competitive. If **ii** is formed then **i** can be reformed, though endergonically, such that the lost azide could be activated by another Fe(OR)$_2$ equivalent to make **i** irreversibly (due to N$_2$ loss). Moreover, this proposed mechanism is consistent with the formation of mixed azoarenes in an approximately statistical ratio from tetrazene under heating. While this

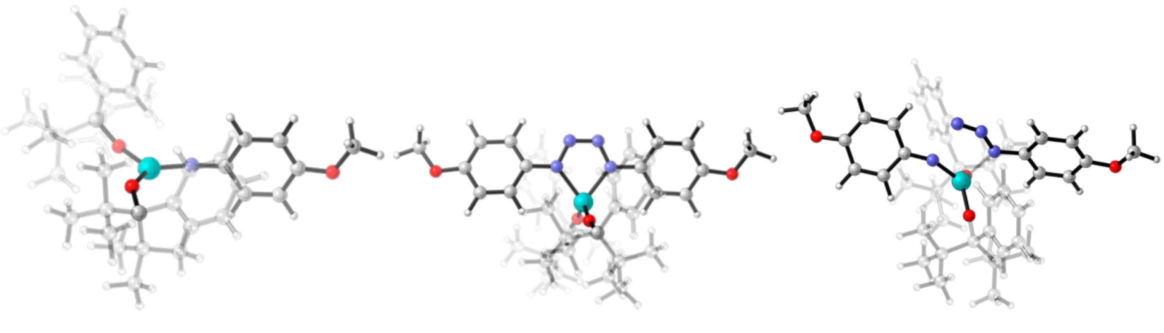

Figure 11. Optimized structures of the quintet iron imido (**i**, left), tetrazene (**ii**, middle), and transition state between these structures (**i**−**ii**−**TS**, right). Solid atoms are those included in the QM region, while those that are partially transparent are in the MM region.[46]

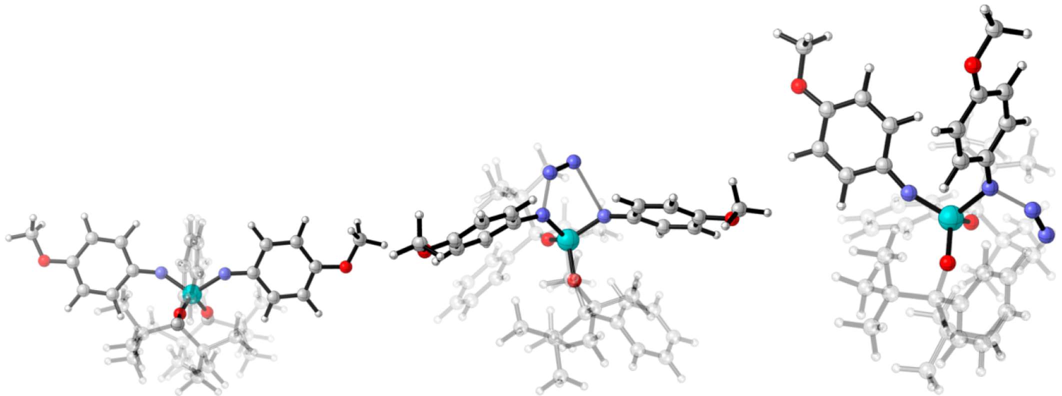

Figure 12. Optimized structures of the quintet iron bis(imido) (**iii**, left), tetrazene (**ii–iii–TS**, middle), and transition state between these structures (**i–iii–TS**, right). Solid atoms are those included in the QM region, while those that are partially transparent are in the MM region.[46]

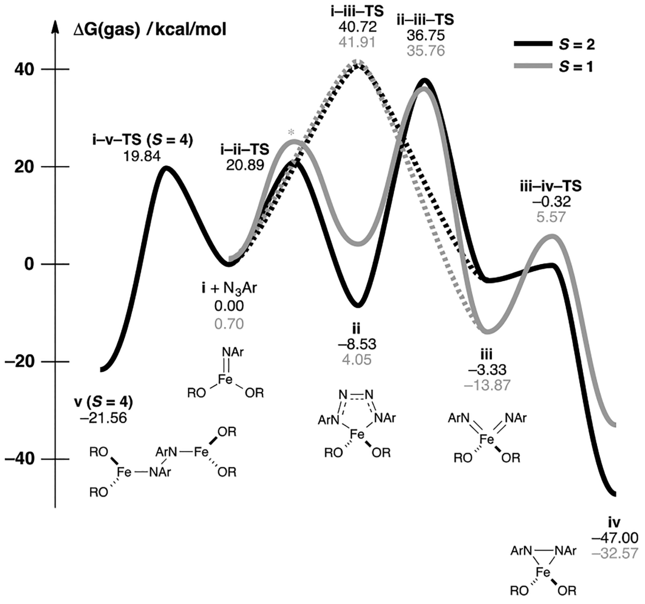

Figure 13. Summary of reaction thermodynamics for the formation of tetrazene and azoarene from **i** and azide. The transition state labeled with * was unable to be located. OR = $OC(^tBu)_2Ph$ and Ar = 4-methoxyphenyl.

mechanism has been probed with the first-generation alkoxide ligand, as shown in Figure S11.1 the reaction thermodynamics are nearly identical for the second-generation alkoxide ligand used in all the experiments in this manuscript. Future work will attempt to unravel the specifics of the aryl azide substitution pattern and more clearly define the role of the alkoxide ligand, using these and similar models.

4. CONCLUSIONS

Our previous work has shown that a monomeric iron bis(alkoxide) complex $Fe(OR)_2(THF)_2$ ($OR = OC^tBu_2Ph$) catalyzed homocoupling of aryl nitrenes to give azoarenes. However, this reactivity was limited to bulky (featuring two groups in the *ortho* positions) aryl azides only; no coupling was observed for the less bulky precursors. In the present work, we demonstrate that the increase in the size of the alkoxide ligand in $Fe(OR')_2(THF)_2$ ($OR' = OC^tBu_2(3,5\text{-}Ph_2Ph)$) enables a significantly broader range of reactivity. Both bulky and nonbulky aryl nitrenes are coupled with $Fe(OR')_2(THF)_2$, albeit the coupling of the less bulky substrates requires higher temperatures and longer reaction times. We explain this difference in reactivity by the increased stability of the $Fe(OR')_2$-type system: while $Fe(OR)_2$ catalysts disproportionated to catalytically inactive mono(alkoxide) and tris(alkoxide) species, only catalytically competent bis(alkoxide) complexes were observed for [OR′]. No reaction intermediates were observed for the $Fe(OR)_2(THF)_2$ system. In contrast, stoichiometric reactions of $Fe(OR')_2(THF)_2$ with nonbulky aryl azides led to the observation of the iron(III) tetrazene radical anion complexes, whose electronic structure was interrogated by field-dependent ^{57}Fe Mössbauer spectroscopy and high-frequency EPR spectroscopy. The relevance of the isolable tetrazene complexes to the reaction mechanism is demonstrated by stoichiometric experiments, in which tetrazene complexes produce azoarene products. Tetrazene complexes likely serve as a "masked form" of the reactive nitrene complex based on these observations and the QM/MM modeling of the reaction mechanism. These calculations suggest that the tetrazene complex is more stable than nitrene and free azide by 8.5 kcal/mol, which may explain the sluggish reactivity of the less bulky aryl azides. Our future studies will focus on the related iron chemistry with a chelating bis(alkoxide) ligand, which will further increase the stability of the system and lead to better catalysis.

■ ASSOCIATED CONTENT

Ⓢ Supporting Information

The Supporting Information is available free of charge on the ACS Publications website at DOI: 10.1021/acs.inorgchem.8b01418.

> Additional Mössbauer spectra, HFEPR spectra, NMR spectra, GC-MS spectra, and computational results (PDF)

Accession Codes

CCDC 1844108−1844110 contain the supplementary crystallographic data for this paper. These data can be obtained free of charge via www.ccdc.cam.ac.uk/data_request/cif, or by emailing data_request@ccdc.cam.ac.uk, or by contacting The Cambridge Crystallographic Data Centre, 12 Union Road, Cambridge CB2 1EZ, UK; fax: +44 1223 336033.

■ AUTHOR INFORMATION

Corresponding Authors

*(S.G.) E-mail: groysman@chem.wayne.edu.

*(S.S.) E-mail: sstoian@uidaho.edu.
*(R.L.L.) E-mail: lordri@gvsu.edu.

ORCID

Andrew Ozarowski: 0000-0001-6225-9796
Sebastian A. Stoian: 0000-0003-3362-7697
Richard L. Lord: 0000-0001-6692-0369
Stanislav Groysman: 0000-0003-3578-7985

Present Address

⊥Lumigen Instrument Center, Wayne State University, 5101 Cass Avenue, Detroit, Michigan 48202, United States

Notes

The authors declare no competing financial interest.

■ ACKNOWLEDGMENTS

S.G. gratefully acknowledges support from the National Science Foundation under Grant Number CHE-1349048. A portion of this work was performed at the National High Magnetic Field Laboratory, which is supported by the National Science Foundation Cooperative Agreement No. DMR-1157490 and the State of Florida. Some of the Mössbauer instrumentation was purchased using a NHFML User Collaboration Grant Program (UCGP-5064 to A.O.). C.D.H., E.W.-S., and R.L.L. were financially supported by a Cottrell College Science Award to R.L.L. R.L.L. acknowledges an NSF MRI CH3-1039925 for computational resources granted to the Midwest Undergraduate Computational Chemistry Consortium. S.A.S. acknowledges partial support from the University of Idaho. We thank the Lumigen Instrument Center for the use of their Mass Spectrometry and NMR resources.

■ REFERENCES

(1) (a) Hunger, K. *Industrial Dyes: Chemistry, Properties, Applications*, 3rd ed.; Wiley-VCH: Weinheim, Germany, 2003.

(2) Feringa, B. L.; Van Delden, R. A.; Koumura, N.; Geertsema, E. M. Chiroptical Molecular Switches. *Chem. Rev.* **2000**, *100*, 1789−1816.

(3) Ikeda, T.; Tsutsumi, O. Optical switching and image storage by means of azobenzene liquid-crystal films. *Science* **1995**, *268*, 1873−1875.

(4) (a) Jain, A.; Gupta, Y.; Jain, S. K. Azo chemistry and its potential for colonic delivery. *Crit. Rev. Ther. Drug Carrier Syst.* **2006**, *23*, 349. (b) Harnoy, A. J.; Slor, G.; Tirosh, E.; Amir, R. J. The effect of photoisomerization on the enzymatic hydrolysis of polymeric micelles bearing photo-responsive azobenzene groups at their cores. *Org. Biomol. Chem.* **2016**, *14*, 5813−5819.

(5) Merino, E. Synthesis of azobenzenes: the coloured pieces of molecular materials. *Chem. Soc. Rev.* **2011**, *40*, 3835−3853.

(6) *Organic Azides: Synthesis and Applications*; Bräse, S.; Banert, K., Eds.; John Wiley and Sons: Chichester, West Sussex, United Kingdom, 2010.

(7) For selected reviews on middle and late-metal imido complexes, see: (a) Eikey, R. A.; Abu-Omar, M. M. Nitrido and imido transition metal complexes of Groups 6−8. *Coord. Chem. Rev.* **2003**, *243*, 83−124. (b) Berry, J. F. Terminal Nitrido and Imido Complexes of the Late Transition Metals. *Comments Inorg. Chem.* **2009**, *30*, 28−66. (c) Ray, K.; Heims, F.; Pfaff, F. F. Terminal Oxo and Imido Transition-Metal Complexes of Groups 9−11. *Eur. J. Inorg. Chem.* **2013**, *2013*, 3784−3807.

(8) (a) For selected recent references on isolated late-metal imido complexes, see: (a) Wilding, M. J. T.; Iovan, D. A.; Betley, T. A. High spin iron imido complexes competent for C-H bond amination. *J. Am. Chem. Soc.* **2017**, *139*, 12043. (b) Laskowski, C. A.; Miller, A. J. M.; Hillhouse, G. L.; Cundari, T. R. A two-coordinate nickel imido complex that effects C−H amination. *J. Am. Chem. Soc.* **2011**, *133*, 771−773. (c) Zhang, L.; Liu, Y.; Deng, L. Three-Coordinate Cobalt(IV) and Cobalt(V) Imido Complexes with N-Heterocyclic Carbene Ligation: Synthesis, Structure, and Their Distinct Reactivity in C−H Bond Amination. *J. Am. Chem. Soc.* **2014**, *136*, 15525−15528. (d) Cowley, R. E.; DeYonker, N. J.; Eckert, N. A.; Cundari, T. R.; DeBeer, S.; Bill, E.; Ottenwaelder, X.; Flaschenriem, C.; Holland, P. L. Three-Coordinate Terminal Imidoiron(III) Complexes: Structure, Spectroscopy, and Mechanism of Formation. *Inorg. Chem.* **2010**, *49*, 6172−6187. (e) Aguila, M. J.; Badiei, Y. M.; Warren, T. H. Mechanistic Insights into C-H Amination via Dicopper Nitrenes. *J. Am. Chem. Soc.* **2013**, *135*, 9399−9406. (f) Searles, K.; Fortier, S.; Khusniyarov, M.; Carroll, P. J.; Sutter, J.; Meyer, K.; Mindiola, D. J.; Caulton, K. G. A cis-Divacant Mononuclear Iron(IV) Imide. *Angew. Chem., Int. Ed.* **2014**, *53*, 14139−14143.

(9) For selected recent reviews on C-H bond activation with organoazide precursors, see: (a) Zhang, L.; Deng, L. C−H bond amination by iron-imido/nitrene species. *Chin. Sci. Bull.* **2012**, *57*, 2352−2360. (b) Driver, T. G. Recent advances in transition metal-catalyzed N-atom transfer reactions of azides. *Org. Biomol. Chem.* **2010**, *8*, 3831−3846.

(10) For selected recent review on aziridination with organoazide precursors, see: Jenkins, D. M. Atom-Economical C2 + N1 Aziridination: Progress towards Catalytic Intermolecular Reactions Using Alkenes and Aryl Azides. *Synlett* **2012**, *23*, 1267−1270.

(11) For selected references on the catalytic formation of carbodiimides using organoazide precursors, see: (a) Cowley, R. E.; Golder, M. R.; Eckert, N. A.; Al-Afyouni, M. H.; Holland, P. L. Mechanism of Catalytic Nitrene Transfer Using Iron(I)−Isocyanide Complexes. *Organometallics* **2013**, *32*, 5289−5298. (b) Wiese, S.; Aguila, M. J. B.; Kogut, E.; Warren, T. H. β-Diketiminato Nickel Imides in Catalytic Nitrene Transfer to Isocyanides. *Organometallics* **2013**, *32*, 2300−2308. (c) Yousif, M.; Tjapkes, D. J.; Lord, R. L.; Groysman, S. Catalytic Formation of Asymmetric Carbodiimides at Mononuclear Chromium (II/IV) Bis(alkoxide) Complexes. *Organometallics* **2015**, *34*, 5119−5128.

(12) Ragaini, F.; Penoni, A.; Gallo, E.; Tollari, S.; Li Gotti, C.; Lapadula, M.; Mangioni, E.; Cenini, S. Amination of Benzylic C[BOND]H Bonds by Arylazides Catalyzed by CoII−Porphyrin Complexes: A Synthetic and Mechanistic Study. *Chem. - Eur. J.* **2003**, *9*, 249−259.

(13) Harrold, N. D.; Waterman, R.; Hillhouse, G. L.; Cundari, T. R. Group-Transfer Reactions of Nickel−Carbene and − Nitrene Complexes with Organoazides and Nitrous Oxide that Form New C═N, C═O, and N═N Bonds. *J. Am. Chem. Soc.* **2009**, *131*, 12872−12873.

(14) (a) Mankad, N. P.; Müller, P.; Peters, J. C. Catalytic N-N Coupling of Aryl Azides To Yield Azoarenes via Trigonal Bipyramid Iron-Nitrene Intermediates. *J. Am. Chem. Soc.* **2010**, *132*, 4083−4085. (b) Takaoka, A.; Moret, M.-E.; Peters, J. C. A Ru(I) Metalloradical That Catalyzes Nitrene Coupling to Azoarenes from Arylazides. *J. Am. Chem. Soc.* **2012**, *134*, 6695−6706.

(15) Heyduk, A. F.; Zarkesh, R. A.; Nguyen, A. I. Designing Catalysts for Nitrene Transfer Using Early Transition Metals and Redox-Active Ligands. *Inorg. Chem.* **2011**, *50*, 9849−9863.

(16) Powers, I. G.; Andjaba, J. M.; Luo, X.; Mei, J.; Uyeda, C. Catalytic Azoarene Synthesis from Aryl Azides Enabled by a Dinuclear Ni Complex. *J. Am. Chem. Soc.* **2018**, *140*, 4110−4118.

(17) (a) Bellow, J. A.; Yousif, M.; Groysman, S. Discrete Complexes of 3d Metals with Monodentate Bulky Alkoxide Ligands and Their Reactivity in Bond Activation and Bond Formation Reactions. *Comments Inorg. Chem.* **2016**, *36*, 92−122. (b) Bellow, J. A.; Fang, D.; Kovacevic, N.; Martin, P. D.; Shearer, J.; Cisneros, G. A.; Groysman, S. Novel Alkoxide Cluster Topologies Featuring Rare Seesaw Geometry at Transition Metal Centers. *Chem. - Eur. J.* **2013**, *19*, 12225−12228. (c) Bellow, J. A.; Martin, P. D.; Lord, R. L.; Groysman, S. Reductive Coupling of Azides Mediated by an Iron(II) Bis(alkoxide) Complex. *Inorg. Chem.* **2013**, *52*, 12335−12337. (d) Bellow, J. A.; Yousif, M.; Fang, D.; Kratz, E. G.; Cisneros, G. A.; Groysman, S. Synthesis and Reactivity of 3d Metal Complexes

with the Bulky Alkoxide Ligand [OC^{t}Bu$_2$Ph]. *Inorg. Chem.* **2015**, *54*, 5624−5633. (e) Bellow, J. A.; Stoian, S. A.; Van Tol, J.; Ozarowski, A.; Lord, R. L.; Groysman, S. Synthesis and Characterization of a Stable High-Valent Cobalt Carbene Complex. *J. Am. Chem. Soc.* **2016**, *138*, 5531−5534.

(18) Bellow, J. A.; Yousif, M.; Cabelof, A. C.; Lord, R. L.; Groysman, S. Reactivity Modes of an Iron Bis(alkoxide) Complex with Aryl Azides: Catalytic Nitrene Coupling vs Formation of Iron(III) Imido Dimers. *Organometallics* **2015**, *34*, 2917−2923.

(19) Yousif, M.; Cabelof, A. C.; Martin, P. D.; Lord, R. L.; Groysman, S. Synthesis of a Mononuclear, Non-Square-Planar Chromium(II) Bis(alkoxide) Complex and its Reactivity Toward Organic Carbonyls and CO$_2$. *Dalton Trans.* **2016**, *45*, 9794−9804.

(20) Boechat, N.; Ferreira, V. F.; Ferreira, S. B.; Ferreira, M. D. L. G.; da Silva, F. d. C.; Bastos, M. M.; Costa, M. d. S.; Lourenco, M. C. S.; Pinto, A. C.; Krettli, A. U.; Aguiar, A. C.; Teixeira, B. M.; da Silva, N. V.; Martins, P. R. C.; Bezerra, F. A. F. M.; Camilo, A. L. S.; da Silva, G. P.; Costa, C. C. P. Novel 1,2,3-Triazole Derivatives for Use against Mycobacterium tuberculosis H37Rv (ATCC 27294) Strain. *J. Med. Chem.* **2011**, *54*, 5988−5998.

(21) Xu, S.; Zhuang, X.; Pan, X.; Zhang, Z.; Duan, L.; Liu, Y.; Zhang, L.; Ren, X.; Ding, K. 1-Phenyl-4-benzoyl-1H-1,2,3-triazoles as Orally Bioavailable Transcriptional Function Suppressors of Estrogen-Related Receptor α. *J. Med. Chem.* **2013**, *56*, 4631−4640.

(22) Stokes, B. J.; Jovanović, B.; Dong, H.; Richert, K. J.; Riell, R. D.; Driver, T. G. Rh$_2$(II)-Catalyzed Synthesis of Carbazoles from Biaryl Azides. *J. Org. Chem.* **2009**, *74*, 3225−3228.

(23) (a) Olmstead, M. M.; Power, P. P.; Shoner, S. C. Three-coordinate iron complexes: X-ray structural characterization of the amide-bridged dimers [Fe(NR$_2$)$_2$]$_2$ (R = SiMe$_3$, C6H5) and the adduct Fe[N(SiMe$_3$)$_2$]$_2$(THF) and determination of the association energy of the monomer Fe(N(SiMe$_3$)$_2$)$_2$ in solution. *Inorg. Chem.* **1991**, *30*, 2547−2551. (b) Deschner, T.; Törnroos, K. W.; Anwander, R. Iron Silylamide-Grafted Periodic Mesoporous Silica. *Inorg. Chem.* **2011**, *50* (15), 7217−7228. (c) Broere, D. L. J.; Čorić, I.; Brosnahan, A.; Holland, P. L. Quantitation of the THF Content in Fe[N-(SiMe3)2]2·xTHF. *Inorg. Chem.* **2017**, *56*, 3140−3143.

(24) Evans, D. F. 400. The determination of the paramagnetic susceptibility of substances in solution by nuclear magnetic resonance. *J. Chem. Soc.* **1959**, 2003−2005.

(25) (a) Gütlich, P.; Bill, E.; Trautwein, A. X. *Mössbauer Spectroscopy and Transition Metal Chemistry: Fundamentals and Applications*; Springer-Verlag: Berlin Heidelberg, 2011. (b) Greenwood, N. N.; Gibb, T. C. *Mössbauer Spectroscopy*; Chapman and Hall: London, 1971.

(26) Hassan, A. K.; Pardi, L. A.; Krzystek, J.; Sienkiewicz, P.; Goy, M.; Rohrer, L.-C; Brunel, L.-C. *J. Magn. Reson.* **2000**, *142*, 300−312.

(27) Frisch, M. J.; Trucks, G. W.; Schlegel, H. B.; Scuseria, G. E.; Robb, M. A.; Cheeseman, J. R.; Scalmani, G.; Barone, V.; Mennucci, B.; Petersson, G. A.; Nakatsuji, H.; Caricato, M.; Li, X.; Hratchian, H. P.; Izmaylov, A. F.; Bloino, J.; Zheng, G.; Sonnenberg, J. L.; Hada, M.; Ehara, M.; Toyota, K.; Fukuda, R.; Hasegawa, J.; Ishida, M.; Nakajima, T.; Honda, Y.; Kitao, O.; Nakai, H.; Vreven, T.; Montgomery, J. A., Jr.; Peralta, J. E.; Ogliaro, F.; Bearpark, M.; Heyd, J. J.; Brothers, E.; Kudin, K. N.; Staroverov, V. N.; Kobayashi, R.; Normand, J.; Raghavachari, K.; Rendell, A.; Burant, J. C.; Iyengar, S. S.; Tomasi, J.; Cossi, M.; Rega, N.; Millam, J. M.; Klene, M.; Knox, J. E.; Cross, J. B.; Bakken, V.; Adamo, C.; Jaramillo, J.; Gomperts, R.; Stratmann, R. E.; Yazyev, O.; Austin, A. J.; Cammi, R.; Pomelli, C.; Ochterski, J. W.; Martin, R. L.; Morokuma, K.; Zakrzewski, V. G.; Voth, G. A.; Salvador, P.; Dannenberg, J. J.; Dapprich, S.; Daniels, A. D.; Farkas, O.; Foresman, J. B.; Ortiz, J. V.; Cioslowski, J.; Fox, D. J. *Gaussian 09 Reference*, Revision D.01; Gaussian, Inc.: Wallingford, CT, 2013.

(28) (a) Vosko, S. H.; Wilk, L.; Nusair, M. Accurate spin-dependent electron liquid correlation energies for local spin density calculations: a critical analysis. *Can. J. Phys.* **1980**, *58*, 1200−1211. (b) Becke, A. D. Density-functional exchange-energy approximation with correct asymptotic behavior. *Phys. Rev. A: At., Mol., Opt. Phys.* **1988**, *38*, 3098−3100. (c) Lee, C.; Yang, W.; Parr, R. G. Development of the Colle-Salvetti correlation-energy formula into a functional of the electron density. *Phys. Rev. B: Condens. Matter Mater. Phys.* **1988**, *37*, 785−789. (d) Becke, A. D. Density-functional thermochemistry. III. The role of exact exchange. *J. Chem. Phys.* **1993**, *98*, 5648−5652. (e) Stephens, P. J.; Devlin, F. J.; Chabalowski, C. F.; Frisch, M. J. Ab Initio Calculation of Vibrational Absorption and Circular Dichroism Spectra Using Density Functional Force Fields. *J. Phys. Chem.* **1994**, *98*, 11623−11627.

(29) Noodleman, L.; Baerends, E. J. Electronic structure, magnetic properties, ESR, and optical spectra for 2-iron ferredoxin models by LCAO-X.alpha. valence bond theory. *J. Am. Chem. Soc.* **1984**, *106*, 2316−2327.

(30) Vrăjmasu, V.; Münck, E.; Bominaar, E. L. Density Functional Study of the Electric Hyperfine Interactions and the Redox-Structural Correlations in the Cofactor of Nitrogenase. Analysis of General Trends in ^{57}Fe Isomer Shifts. *Inorg. Chem.* **2003**, *42*, 5974−5988.

(31) (a) Perdew, J. P.; Burke, K.; Ernzerhof, M. Generalized Gradient Approximation Made Simple. *Phys. Rev. Lett.* **1996**, *77*, 3865−3868. (b) Handy, N. C.; Cohen, A. J. Left-Right Correlation Energy. *Mol. Phys.* **2000**, *99*, 403−412. (c) Swart, M. Accurate Spin-State Energies for Iron Complexes. *J. Chem. Theory Comput.* **2008**, *4*, 2057−2066. (d) Dapprich, S.; Komáromi, I.; Byun, K. S.; Morokuma, K.; Frisch, M. J. *J. Mol. Struct.: THEOCHEM* **1999**, *461*−*462*, 1−21. (e) Chung, L. W.; Sameera, W. M. C.; Ramozzi, R.; Page, A. J.; Hatanaka, M.; Petrova, G. P.; Harris, T. V.; Li, X.; Ke, Z.; Liu, F.; Li, H.-B.; Ding, L.; Morokuma, K. The ONIOM Method and its Applications. *Chem. Rev.* **2015**, *115*, 5678−5796.

(32) (a) Vreven, T.; Frisch, M. J.; Kudin, K. N.; Schlegel, H. B.; Morokuma, K. Geometry optimization with QM/MM methods II: Explicit quadratic coupling. *Mol. Phys.* **2006**, *104*, 701−714. (b) Vreven, T.; Byun, K. S.; Komáromi, I.; Dapprich, S.; Montgomery, J. A., Jr.; Morokuma, K.; Frisch, M. J. Combining Quantum Mechanics Methods with Molecular Mechanics Methods in ONIOM. *J. Chem. Theory Comput.* **2006**, *2*, 815−826.

(33) (a) Bradley, D. C., Mehrotra, R. C., Rothwell, I., Singh, A. *Alkoxo and Aryloxo Derivatives of Metals*; Academic Press: London, 2001. (b) Bartlett, R. A.; Ellison, J. J.; Power, P. P.; Shoner, S. C. *Inorg. Chem.* **1991**, *30*, 2888−2894.

(34) Trogler, W. C. Synthesis, electronic structure, and reactivity of metallacyclotetraazapentadienes. *Acc. Chem. Res.* **1990**, *23*, 426−431.

(35) Cowley, R. E.; Bill, E.; Neese, F.; Brennessel, W. W.; Holland, P. L. Iron(II) Complexes with Redox-Active Tetrazene (RNNNNR) Ligands. *Inorg. Chem.* **2009**, *48*, 4828−4836.

(36) Bellows, S. M.; Brennessel, W. W.; Holland, P. L. Effects of Ligand Halogenation on the Electron Localization, Geometry and Spins State of Low-Coordinate (β-Diketiminato)iron Complexes. *Eur. J. Inorg. Chem.* **2016**, *2016*, 3344−3355.

(37) Mock, M. T.; Popescu, C. V.; Yap, G. P. A.; Dougherty, W. G.; Riordan, C. G. Monovalent Iron in a Sulfur-Rich Environment. *Inorg. Chem.* **2008**, *47*, 1889−1891.

(38) Cramer, S. A.; Hernández Sanchez, R. A.; Brakhage, D.; Jenkins, D. M. Probing the role of an Fe^{IV} tetrazene in catalytic aziridation. *Chem. Commun.* **2014**, *50*, 13967−13970.

(39) Bowman, A. C.; Tondreau, A. M.; Lobkovsky, E.; Margulieux, G. W.; Chirik, P. J. Synthesis and Electronic Structure Diversity of Pyridine(diimine)iron Tetrazene Complexes. *Inorg. Chem.* **2018**, ASAP. DOI: DOI: 10.1021/acs.inorgchem.8b00140.

(40) Stoian, S. A.; Xue, G.; Bominaar, E. L.; Que, L., Jr.; Münck, E. Spectroscopic and Theoretical Investigation of a Complex with an [O═Fe^{IV}-O-Fe^{IV}═O] Core Related to Methane Monooxygenase Intermediate Q. *J. Am. Chem. Soc.* **2014**, *136*, 1545−1558.

(41) Gismelseed, A.; Bominaar, E. L.; Bill, E.; Trautwein, A. X.; Winkler, H.; Nasri, H.; Doppelt, P.; Mandon, J.; Weiss, F. R.; Fischer, J. Six-Coordinate Quantum-Mechanically Weakly Spin-Mixed (S = 5/2, 3/2) (triflato)aquairon(III) "Picket-Fence" Porphyrin Complex: Synthesis and Structural, Mössbauer, EPR, and Magnetic Characterization. *Inorg. Chem.* **1990**, *29*, 2741−2749.

(42) Fitzsimmons, B. W.; Johnson, C. E. The Mössbauer Spectrum of a Three-Coordinate Compound, tris (hexamethyldisilylaminato) iron(III), Fe[N(SiMe$_3$)$_2$]$_3$. *Chem. Phys. Lett.* **1974**, *24*, 422−424.

(43) Gehrmann, T.; Lloret Fillol, J.; Wadepohl, H.; Gade, L. H. Synthesis, Characterization, and Thermal Rearrangement of Zirconium Tetraazadienyl and Pentaazadienyl Complexes. *Organometallics* **2012**, *31*, 4504−4515.

(44) Elpitiya, G. R.; Malbrecht, B. J.; Jenkins, D. M. A Chromium(II) Tetracarbene Complex Allows Unprecedented Oxidative Group Transfer. *Inorg. Chem.* **2017**, *56*, 14101−14110.

(45) Vaddypally, S.; McKendry, I. G.; Tomlinson, W.; Hooper, J. P.; Zdilla, M. J. Electronic Structure of Manganese Complexes of the Redox-Non-innocent Tetrazene Ligand and Evidence for the Metal-Azide/Imido Cycloaddition Intermediate. *Chem. - Eur. J.* **2016**, *22*, 10548−10557.

(46) Legault, C. Y. *CYLview, 1.0b*; Université de Sherbrooke, 2009; http://www.cylview.org.

DOI: 10.1021/acs.inorgchem.8b01418
Inorg. Chem. 2018, 57, 9425−9438